

## Improvements to an ion orbit loss calculation in the tokamak edge

T. M. Wilks and W. M. Stacey

Citation: *Physics of Plasmas* **23**, 122505 (2016); doi: 10.1063/1.4968219

View online: <http://dx.doi.org/10.1063/1.4968219>

View Table of Contents: <http://scitation.aip.org/content/aip/journal/pop/23/12?ver=pdfcov>

Published by the *AIP Publishing*

---

### Articles you may be interested in

[Effect of the plasma shapes on intrinsic rotation due to collisionless ion orbit loss in the tokamak edge plasmas](#)  
*Phys. Plasmas* **21**, 072505 (2014); 10.1063/1.4889898

[Effect of ion orbit loss on the structure in the H-mode tokamak edge pedestal profiles of rotation velocity, radial electric field, density, and temperature](#)  
*Phys. Plasmas* **20**, 092508 (2013); 10.1063/1.4820954

[Tokamak-edge toroidal rotation due to inhomogeneous transport and geodesic curvature](#)  
*Phys. Plasmas* **19**, 055908 (2012); 10.1063/1.4718335

[Modeling the response of a fast ion loss detector using orbit tracing techniques in a neutral beam prompt-loss study on the DIII-D tokamak](#)  
*Rev. Sci. Instrum.* **81**, 10D305 (2010); 10.1063/1.3478996

[The physics of edge resonant magnetic perturbations in hot tokamak plasmas](#)  
*Phys. Plasmas* **13**, 056121 (2006); 10.1063/1.2177657

---



**COMPLETELY  
REDESIGNED!**



*Physics Today* Buyer's Guide  
Search with a purpose.

# Improvements to an ion orbit loss calculation in the tokamak edge

T. M. Wilks and W. M. Stacey

Georgia Institute of Technology, Atlanta, Georgia 30332, USA

(Received 27 June 2016; accepted 31 October 2016; published online 7 December 2016)

An existing model of collisionless particle, momentum, and energy ion orbit loss from the edge region of a diverted tokamak plasma has been extended. The extended ion orbit loss calculation now treats losses of both thermal ions and fast neutral beam injection ions and includes realistic flux surface and magnetic field representations, particles returning to the plasma from the scrape off layer, and treatment of x-transport and x-loss. More realistic flux surface geometry allows the intrinsic rotation calculation to predict a peaking in the profile closer to the separatrix, which is consistent with experiment; and particle tracking calculations reveal a new mechanism of “x-transport pumping,” which predicts larger ion losses when coupling conventional ion orbit loss and x-loss mechanisms, though still dominated by conventional ion orbit loss. Sensitivity to these ion orbit loss model enhancements is illustrated by fluid predictions of neoclassical rotation velocities and radial electric field profiles, with and without the enhancements. *Published by AIP Publishing.*

[<http://dx.doi.org/10.1063/1.4968219>]

## I. INTRODUCTION

There are many indications that tokamak fusion plasma performance in the reactor core will be determined largely by the physics in the far edge region.<sup>1–6</sup> In H-mode plasmas, this far edge region is called the “edge pedestal” due to the steep gradients in the radial density, temperature, current, and pressure profiles, which influence the main plasma energy confinement and stability. These steep gradients observed in the H-mode edge result in higher plasma densities and temperatures in both the edge and plasma core, leading to overall improved plasma performance. Often referred to as an edge “transport barrier,” this steep gradient region is characterized by strong electromagnetic forces and kinetic particle losses. The usual fluid theory is not sufficient to represent the effect of these phenomena on particle transport but must be extended to treat non-diffusive electromagnetic “pinch” forces<sup>7</sup> and ion orbit loss (IOL)<sup>8</sup> of particles on orbits which cross the separatrix.

There is also evidence of strong reduction in turbulent transport suppressed by ExB shear<sup>9,10</sup> in this edge transport barrier, which has been argued to lead to a transition to the improved H-mode confinement regime and is often associated with an increased radial electric field,  $E_r$ , in the edge pedestal region.<sup>11–13</sup>

While this L-H transition has been extensively studied and understood relatively well qualitatively, there is still a need for predictive models that can characterize  $E_r$  in current plasmas as well as in future devices. Along with the L-H transition, changes in the edge radial electric field are also correlated with changes in many edge phenomena such as rotation, transport, and the suppression of large magnetohydrodynamic (MHD) instabilities called Edge Localized Modes (ELMs).<sup>14–18</sup> While the critical gradients and values for these events to occur are set by other mechanisms, such as the peeling-ballooning MHD instability threshold for ELMs and particle and energy sources and sinks for transport properties, all processes must be constrained by conservation equations.

Recently, ion orbit loss of thermalized ions causing highly non-Maxwellian distribution functions in the far edge, along with compensating return currents and intrinsic rotation, has been shown to play a key role in the formation and structure of the radial electric field.<sup>19,20</sup> There has been significant previous research on ion orbit loss,<sup>21–25</sup> corresponding return currents,<sup>25</sup> and their impact on intrinsic rotation.<sup>26–29</sup> Miyamoto<sup>22</sup> developed an analytical representation for ion orbit loss with the inclusion of a radial electric field, which was extended by Stacey<sup>8</sup> for a computationally attractive formulation for use in predictive or interpretive fluid codes. Mach probe measurements of velocity peaking in DIII-D have spurred numerical simulations by deGrassie<sup>27</sup> and analytical modeling by Stacey<sup>26</sup> to characterize intrinsic rotation from thermal ion losses in the far edge region. Recent XGC0 simulations<sup>30,31</sup> have also supported the theory that ion orbit losses causing highly non-Maxwellian distribution functions greatly impact the radial electric field, which is closely linked to both diffusive and electromagnetic edge transport processes. Thus, it is desirable to develop improved ion orbit loss models which can be leveraged in existing momentum based predictive models for the radial electric field and its influence on the rest of the plasma, as exemplified in References 32 and 33.

This paper extends the ion orbit loss model of References 24 and 8, to account for (1) prompt loss of fast neutral beam ions, (2) realistic flux surface geometry and magnetic fields, (3) return currents from the scrape off layer (SOL), (4) outward streaming lost particles that return to the plasma, and (5) x-transport and x-loss. This improved ion orbit loss methodology is applied to self consistently model radial particle fluxes, intrinsic rotation velocities, and the radial electric field. The paper is organized as follows: Section II introduces the improvements to the ion orbit loss calculation; Section III describes how the ion orbit loss improvements affect the momentum-based methodology for calculating radial particle flux, intrinsic rotations, and the radial electric field; and Section IV presents conclusions and future implications of this research.

## II. ION ORBIT LOSS THEORY AND MODEL IMPROVEMENTS

### A. Basic ion orbit loss theory

Conservation principles are employed to calculate a minimum energy required for ion orbit loss of ions by accessing orbits that cross the separatrix. This calculation does not track particle orbits but determines the physical requirements on ion energy for a particle to execute a loss orbit. A collisionless plasma is assumed, which can be interpreted such that no ions are allowed to scatter into or out of the loss cone calculated by these conservation principles, but there is an outward flowing ion population that has a loss cone with a lower energy boundary that is decreasing with increasing radius.<sup>8</sup> The calculation is based on the conservation of canonical toroidal angular momentum, energy, and magnetic moment

$$R_s m V_{par,s} \left( \frac{B_{\phi,s}}{B_s} \right) + e \psi_s = \text{constant} \\ = R_0 m V_{par,0} \left( \frac{B_{\phi,0}}{B_0} \right) + e \psi_0, \quad (1)$$

$$\frac{1}{2} m (V_{par,s}^2 + V_{perp,s}^2) + e \phi_s = \text{constant} \\ = \frac{1}{2} m (V_{par,0}^2 + V_{perp,0}^2) + e \phi_0, \quad (2)$$

$$\frac{m V_{perp,s}^2}{2 B_s} = \text{constant} = \frac{m V_{perp,0}^2}{2 B_0}. \quad (3)$$

$R$  is the major radius,  $m$  is the mass,  $V$  is velocity,  $B$  is the magnetic field,  $\psi$  is the amount of enclosed poloidal magnetic flux, and  $\phi$  is the electrostatic potential. The subscripts “perp” and “par” refer to directions perpendicular or parallel to the total magnetic field. The “0” subscripts indicate the values of the quantity on a reference internal flux surface,  $\psi_0$ , in the edge region. The second surface required to satisfy

these conservation equations is the separatrix,  $\psi_s$ , denoted by the subscript “s.” Combining these constraints then leads to a quadratic expression defining the minimum speed,  $V_0 = \sqrt{V_{par,0}^2 + V_{perp,0}^2}$ , that an ion with a given direction at a given location on an internal flux surface must have in order to reach a given location on the last closed flux surface,  $\psi_s$

$$V_0^2 \left[ \left( \left| \frac{B_s}{B_0} \right| \frac{f_{\phi,0}}{f_{\phi,s}} \right)^2 - 1 + \left( 1 - \xi_0^2 \right) \left| \frac{B_s}{B_0} \right| \right] \\ + V_0 \left[ \frac{2e(\psi_0 - \psi_s)}{R m f_{\phi,s}} \left( \left| \frac{B_s}{B_0} \right| \frac{f_{\phi,0}}{f_{\phi,s}} \xi_0 \right) \right] \\ + \left[ \left( \frac{e(\psi_0 - \psi_s)}{R m f_{\phi,s}} \right)^2 - \frac{2e(\phi_0 - \phi_s)}{m} \right] = 0. \quad (4)$$

$f_\phi = |B_\phi/B|$  and  $\xi_0$  is the cosine of the initial particle direction with respect to the toroidal magnetic field. This minimum velocity is numerically calculated for each internal flux surface  $\psi_0$  at various poloidal locations, and for several  $\xi_0$  values, which is relevant for both carbon and deuterium, however, only main ion losses will be discussed here for inclusion in fluid equations. Experimental profiles used to evaluate and interpret Eq. (4) for a DIII-D H-mode discharge that will be discussed in Sections II B–II E are shown in Fig. 1.

The minimum energy,  $E_{min} \equiv m V_{0,min}^2 / 2$ , required for deuterium ion orbit loss from the inboard and outboard mid-plane locations on the flux surface at the pedestal top ( $\rho = 0.966$ ) in the H-mode shot is shown in Fig. 2(a) as a function of direction cosine with respect to  $B_\phi$ , or pitch angle  $\xi_0$ . This minimum energy is clearly sufficiently large for co-current ions ( $B_\phi$  and  $I_p$  are oppositely directed in this shot) at the inboard midplane that no co-current particles will be lost, but for counter-current ions the particles in the upper-energy tail of the thermalized distribution may be lost, depending on the local ion temperature (or thermal velocity). This is shown more clearly in Fig. 2(b), where the contours of the ratio of

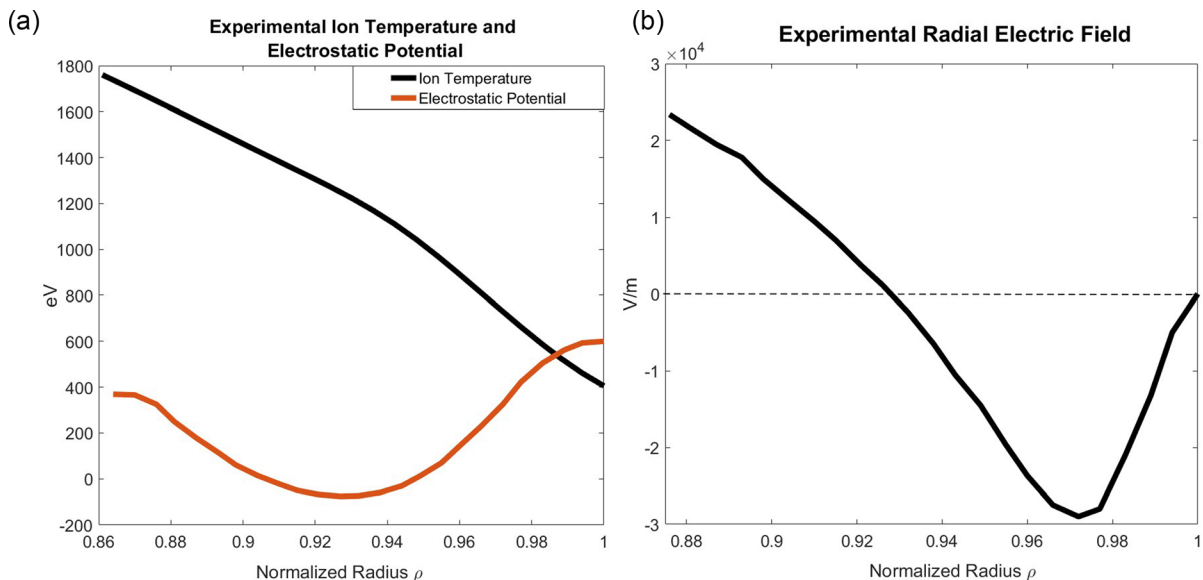


FIG. 1. Experimental profiles of (a) ion temperature and electrostatic potential and (b) radial electric field for DIII-D H-mode discharge #123302 at 2600 ms.

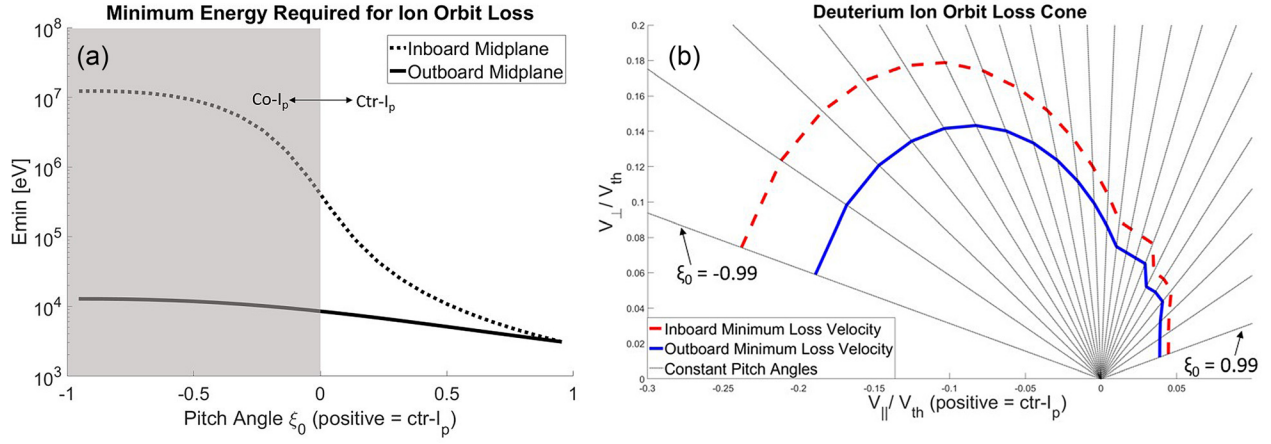


FIG. 2. Minimum energy and velocity required for a deuterium ion to be ion orbit lost at the top of the pedestal ( $\rho = 0.966$ ) at both the inboard and outboard midplane as a function of pitch angle calculated from Equation (4) assuming circular flux surface geometry.

the minimum loss speed to the thermal speed are plotted as a function of  $\xi_0$ . When this ratio is large (as is for co- $I_p$  directed ions) very few, if any, particles are ion orbit lost, but when this ratio is small (as is for ctr- $I_p$  directed ions) particles in the upper energy range of the distribution can be lost.

Consistent with other ion orbit loss models and intrinsic rotation measurements, Fig. 2 illustrates smaller minimum orbit loss energies (2a) and velocities (2b) for ions located at the outboard midplane. The loss of high energy particles truncates the ion distribution above  $E_{min}(\xi_0)$ , and this effect is more pronounced for ctr- $I_p$  directed particles than for co- $I_p$  directed particles and more pronounced at the outboard midplane than the inboard midplane. In general, the contours in Figs. 2(a) and 2(b) will decrease with increasing radius. This is discussed in more detail in References 8 and 34.

Figure 2 agrees qualitatively with the numerical calculation of ion orbit loss using Eqs. (1)–(3) in Reference 23 in that it is the ions with velocity strongly in the direction of the magnetic field ( $\xi_0 \gg 0$ ) that are most likely to be lost. However, Reference 23 uses model radial electric field profiles while Fig. 2 uses the experimental profile (e.g., the electrostatic potential in Fig. 1(a) calculated from the experimental radial electric field  $E_r = -\hat{n}_r - \nabla\phi$  in Fig. 1(b)), and Reference 23 calculates orbits intersecting a specific confinement chamber geometry as lost, whereas a fraction  $R_{loss}$  of the ions crossing the separatrix are treated as lost in this paper, so that a quantitative comparison is not possible.

The cumulative fraction of lost particles out to radius ‘ $r$ ’ can then be calculated<sup>8</sup> by integrating the distribution function over the loss region  $V_0 > V_{0,min}$ , and then integrating over the direction cosine (pitch angle)

$$F_{therm}^{IOL}(r) = \frac{N_{loss}}{N_{total}} = \frac{R_{loss}^{IOL} \int_{-1}^1 \left[ \int_{V_{0,min}}^{\infty} V_0^2 f(V_0) dV_0 \right] d\xi_0}{2 \int_0^{\infty} V_0 f(V_0) dV_0} = \frac{R_{loss}^{IOL} \int_{-1}^1 \Gamma\left(\frac{3}{2}, \epsilon_{min}(\xi_0)\right) d\xi_0}{2\Gamma\left(\frac{3}{2}\right)}. \quad (5)$$

$R_{loss}^{IOL}$  is the fraction of particles that cross the separatrix on loss orbits and do not return to the plasma, which will be discussed later in this section,  $\Gamma$  is the gamma function (arising from the use of a truncated Maxwellian distribution function to evaluate the velocity integral),  $f(V_0)$  is the ion distribution function, and  $\epsilon_{min}(\xi_0) = mV_{0,min}^2(\xi_0)/2kT_{ion}$ . This calculation is fully differential in four dimensions:<sup>34</sup> (1) radial coordinate ( $\rho$ ), (2) initial poloidal location ( $\theta_0$ ), (3) final poloidal location on the separatrix ( $\theta_s$ ), and (4) pitch angle ( $\xi_0$ ), which allows the distribution function to evolve due to the changing velocity loss cone structure in the outer flux surface regions close to the separatrix.

A similar process can be followed for momentum and energy loss fractions, but with moments of  $mV_0\xi_0$  and  $\frac{1}{2}mV_0^2$  applied to the velocity integral, respectively.<sup>8</sup> For example, the momentum loss fraction is

$$M_{therm}^{IOL} = \frac{M_{loss}}{M_{total}} = \frac{R_{loss}^{IOL} \int_{-1}^1 \left[ \int_{V_{0,min}}^{\infty} (mV_0\xi_0) V_0^2 f(V_0) dV_0 \right] d\xi_0}{2 \int_0^{\infty} (mV_0) V_0 f(V_0) dV_0} = \frac{R_{loss}^{IOL} \int_{-1}^1 \xi_0 \Gamma\left(\frac{5}{2}, \epsilon_{min}(\xi_0)\right) d\xi_0}{2\Gamma\left(\frac{5}{2}\right)}. \quad (6)$$

Noting that the total momentum loss from the plasma due to ion orbit loss is the numerator in Eq. (6), an IOL intrinsic rotation for ion species ‘ $j$ ’ in the toroidal direction can be defined for use in calculating the rotation velocity profiles required for the radial electric field calculation

$$\Delta V_{\phi j}^{IOL} = \hat{n}_{\parallel} \cdot \hat{n}_{\phi} \Delta V_{\parallel j}^{IOL} = 2\pi \left| \frac{B_{\phi}}{B_{tot}} \right| \int_{-1}^1 d\xi_0 \left[ \int_{V_{0,min}(\xi_0)}^{\infty} (V_0\xi_0) V_0^2 f(V_0) dV_0 \right] = \frac{2}{\sqrt{\pi}} \left| \frac{B_{\phi}}{B_{tot}} \right| M_{therm}^{IOL} \sqrt{\frac{2kT_j}{m_j}}. \quad (7)$$



It is assumed that the return current ions rejoining the plasma from the “cold” scrape off layer have negligible momentum and do not affect the intrinsic rotation calculation. Theoretically, fast ion losses could also be included in the intrinsic rotation calculation, and MAST experiments have shown that in low aspect ratio machines, there can be more momentum deposited in the plasma than originally injected by neutral beams.<sup>25</sup> However, in this work, a simplified model is used with a multiplier on the co-current neutral beam injected (NBI) momentum, which is presently considered to have a value of 1.0 due to the large aspect ratio of DIII-D.

### B. Ion orbit loss of fast neutral beam ions

Fast ions are accelerated to roughly 80 keV, converted into neutral atoms or molecules of  $D_1$ ,  $D_2$ , or  $D_3$ , and are then launched into the DIII-D plasma for heating, fueling, current drive, and rotational drive. Since there are several molecular species of deuterium, the neutral beam takes three characteristic energies: full energy  $E$  for  $D_1$  atoms, half energy  $E/2$  for  $D_2$  molecules, and third energy  $E/3$  for  $D_3$  molecules, where  $E$  is the acceleration energy. The fraction of the total beam in each energy component has been experimentally determined for DIII-D and can be calculated as a function of the total energy component.<sup>35</sup> For this analysis, the fraction of injected beam particles is approximately 76%, 13%, and 11% for the full, half, and third energy components, respectively.

Fast ion deposition profiles, shown in Fig. 3(a), can be calculated using various numerical codes such as NUBEAM<sup>35</sup> and NBeams,<sup>36</sup> which estimate deposition based on charge exchange and ionization cross sections on each flux surface due to local conditions.

Since each beam follows a straight-line deposition trajectory, there is a characteristic pitch angle or angle of the beam direction with respect to the toroidal magnetic field. Figure 3(b) shows the pitch angle calculated for circular flux surfaces compared to elongated elliptical flux surfaces generated from NBeams ( $\zeta_0 > 0$  for ctr-I,  $\zeta_0 < 0$  for co-I ions).

The elliptical pitch angles were used for the fast neutral beam injected ion orbit loss calculations in this paper.

The ion orbit loss calculation for fast ions can be derived from the formalism in Section II A by treating the pitch angle and velocity distribution in a different manner than for the thermal population. The minimum energy calculation from Eq. (4) takes the pitch angle as an independent variable. For thermal ions, particle trajectories can have any angle with respect to the toroidal magnetic field; therefore, all pitch angles are considered. However, the fast ion calculation requires only one pitch angle for each surface as required by geometry for promptly lost particles. This simplification allows the minimum energy calculation to solely depend on the poloidal angle, instead of both the poloidal angle and the pitch angle as is the case for thermal ions.

Furthermore, the beam energy distribution functions are treated as a delta function centered around three specific energies derived from the injection system and not a Maxwellian distribution as in the thermal ion case. The neutral beam injected (NBI) particles can be seen as a mono-energetic external source of ions onto flux surfaces with a single pitch angle. If minimum energies for each flux surface are calculated, then the fast ion loss fraction simply depends on whether the NBI energy component exceeds the minimum energy requirements for the ions to be ion orbit lost. Fast ions that are promptly lost due to IOL decrease the NBI source term in the continuity equation for thermalized ions. The deposition profile is used to modify the NBI source term for the thermalized ion continuity equation to obtain

$$\hat{S}_{NBI} = \sum_{i=1}^3 \frac{P_{beam}}{E_{beam}^i} \left[ 1 - 2F_{fast}^i(\rho) \right] H^i(\rho), \quad (8)$$

where  $H$  is the normalized neutral beam deposition profile calculated from NBeams and shown in Fig. 3(a). The inward return current compensating the loss of fast ions is assumed to consist of thermalized ions from the scrape off layer, accounting for the factor of 2 in the thermal ion radial particle flux source of Eq. (8). While the thermal ion loss fraction

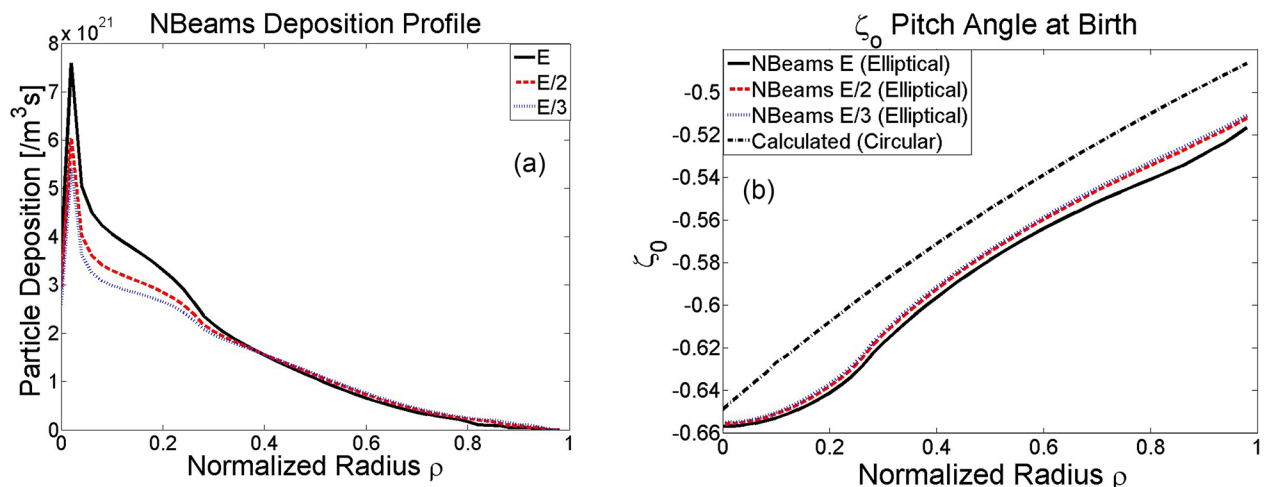


FIG. 3. (a) Neutral beam deposition profiles calculated from NBeams for each energy component. (b) Pitch angle comparisons for elliptical flux surfaces (calculated by NBeams) and for circular flux surfaces.

of Eq. (5) is cumulative in radius, the fast beam ion loss fraction of Eq. (9) is differential at the local radius.

The NBI source rate is summed over all the energy components, where the particle energy, loss fraction, and the deposition profile structure are dependent upon the energy component,  $i$ , representing  $E$ ,  $E/2$ , and  $E/3$ . The fast ion loss fraction is calculated by considering the number of poloidal loss directions for all energy components on each flux surface divided by the total number of poloidal directions

$$F_{fast}(\rho) = \frac{\sum_{i=1}^3 \int_0^\pi \theta \in [E_{min}^i(\rho, \theta) < E_{NBI}^i] d\theta}{\sum_{i=1}^3 \int_0^\pi \theta d\theta}. \quad (9)$$

$\theta \in [E_{min}^i(\rho, \theta) < E_{NBI}^i]$  is the condition requiring fast neutral beam ions to have greater energy than the minimum needed for ion orbit loss to be included in the integral.

Figure 4 shows the loss fractions for the various energy components of fast beam ions compared to the cumulative (in radius) thermalized loss fractions calculated from Eqs. (9) and (5), respectively. The profile structure of the fast ion loss fractions is due to the small number of poloidal loss angles considered numerically, which can be readily extended in future analysis. The fast loss profiles extend farther into the plasma than the thermal loss profiles, suggesting the possibility that for large NBI systems or systems that focus on injecting particles in the edge where these large NBI loss fractions exist may generate significant fast losses which would be coupled with large return currents. Substantial fast ion losses in the edge like this have the potential to generate significant intrinsic rotation and are therefore of great interest for future investigations for situations where direct NBI cannot drive rotation in the usual way.<sup>25</sup>

Fast loss fractions often extend farther into the plasma than the mesh used for edge calculations in this paper. The losses inside of the edge pedestal region (illustrated in Fig. 5(a) in Section II C) are integrated and removed from the

total NBI source, and the edge region fast losses are maintained as a radial function to be included in the continuity equation for thermalized ions.

### C. Use of experimental flux surfaces and magnetic fields

Previous ion orbit loss calculations using the model of References 8 and 34 used a simplified circular geometry to calculate flux surface values as well as parameters like magnetic fields and major radii

$$R(r, \theta) = \bar{R}h(r, \theta), \quad (10a)$$

$$B_{\theta, \phi}(r, \theta) = \frac{\bar{B}_{\theta, \phi}}{h(r, \theta)}, \quad (10b)$$

$$h(r, \theta) = 1 + \frac{r}{\bar{R}} \cos(\theta), \quad (10c)$$

and used Ampere's Law, assuming uniform current density, to define flux surface values

$$\psi = RA_\phi = \frac{\mu_0 I \bar{R} \bar{r}^2}{4\pi \bar{a}^2}, \quad (11)$$

where “I” is the plasma current and “ $\bar{r}$ ” is the effective plasma radius of a circular plasma. The corresponding plasma minor radius is assumed to be that of the effective circular geometry that preserves the area for an elongated elliptical plasma of horizontal dimension  $2a$  and vertical

dimension  $2b$ ,  $\bar{a} = \sqrt{\frac{1}{2} \left( 1 + \left( \frac{b}{a} \right)^2 \right)}$ . Sensitivity of the calculations of Eqs. (4)–(6) to the flux surface geometry treatment can be explored by comparing the results of calculations using measured flux surface geometry with calculations using the circular model. Experimental flux surfaces and magnetic fields obtained from EFIT<sup>37</sup> are shown in Fig. 5, and the circular model flux surface of Eq. (11) is shown for comparison in Fig. 5(b).

Experimental data were also used for the toroidal magnetic field, allowing the minimum energy calculation in Eq. (4) to be evaluated with purely experimental parameters. With these model improvements, Fig. 6 shows the influence of using realistic flux surface geometry and magnetic fields on the loss fraction calculation.

Calculating loss fractions with measured flux surface geometry decreases the total cumulative IOL for particles and energy and changes the structure of the loss profile to show a sharper increase of lost particles in the far edge as opposed to the more gradual loss of particles with the approximate circular model calculation. Momentum losses reflect similar results and are shifted towards the separatrix with a larger and more pronounced peak when using experimental values, which agrees with previous models and experimental observations.<sup>29,31,38</sup>

In order to make this improved model a predictive model, an analytical fit to flux surfaces can be used in lieu of experimental equilibria. Previous analysis<sup>39</sup> has shown that a modified Miller model is an accurate and computationally manageable means to model flux surfaces. The Miller

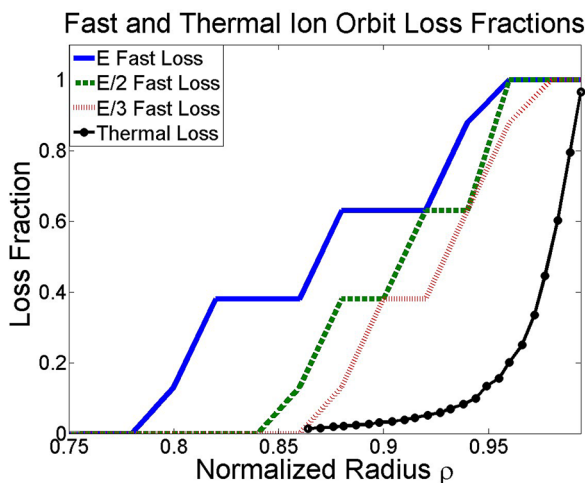


FIG. 4. Ion orbit loss fractions for fast neutral beam particles of different energy components and for thermal ions assuming circular flux surface geometry.

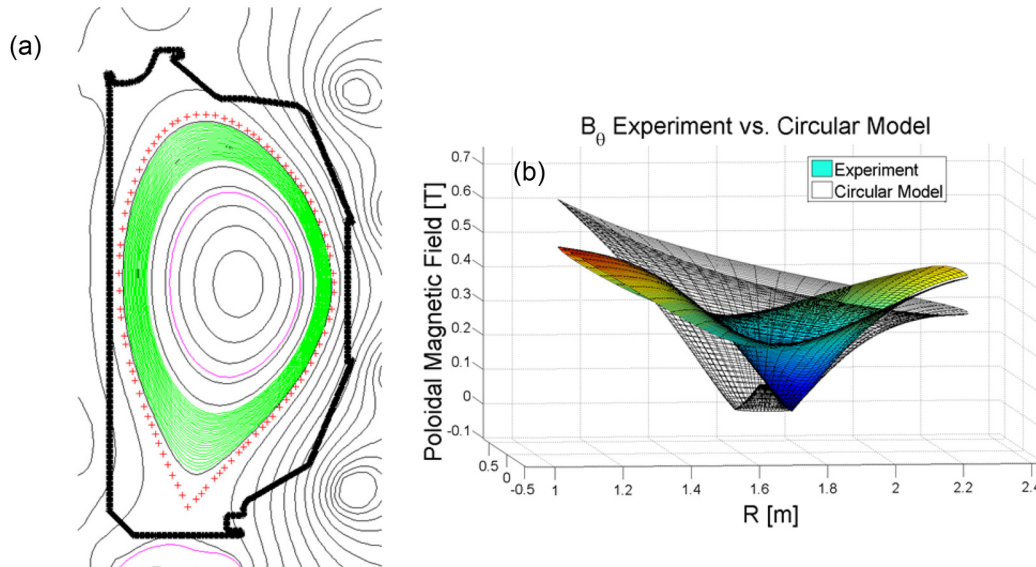


FIG. 5. (a) Experimental flux surfaces in the edge region (shaded) with the separatrix shown by dashed line (b) Experimental poloidal magnetic field (opaque surface) compared to circular model analytical fit (transparent surface).

model<sup>40</sup> is an analytical geometric model that can treat elongated plasma geometries by representing Cartesian (R,Z) coordinates of plasma flux as functions of plasma elongation,  $\kappa$ , and triangularity,  $\delta$

$$R(r, \theta) = R_0 + r \cos \xi, \quad (12a)$$

$$Z(r, \theta) = \kappa r \sin \theta_m, \quad (12b)$$

where  $\xi(r, \theta) = \theta_m + x_\delta(r) \sin \theta_m$ ,  $x_\delta = \sin^{-1} \theta_m$ , and  $\theta_m$  is slightly different from the true poloidal angle and is defined by the triangle with hypotenuse of  $\kappa r$  and height Z. This model was employed to generate a new mesh with more realistic flux surfaces in the outer plasma region for the ion orbit loss calculation (but not for the general plasma balance calculation). These modeled surfaces shown by the grid structure in Fig. 7 represent the experimental flux surfaces much more accurately than a circular model and yield almost identical results to the calculation based on the EFIT (<1% positional error<sup>39</sup>) flux surfaces shown in Fig. 5(a).

The improved flux surface model can be used for both thermal and fast ion loss calculations and then applied to the fluid calculation via 1D loss fraction profiles as a function of normalized radius, so there are no geometric issues with merging the two geometric models.

#### D. Effect of returning particles

Tightly trapped banana orbiting particles satisfy the conservation requirements to be ion orbit lost but may return to the plasma after executing those orbits that cross the separatrix. If the fraction of this number of returning particles to

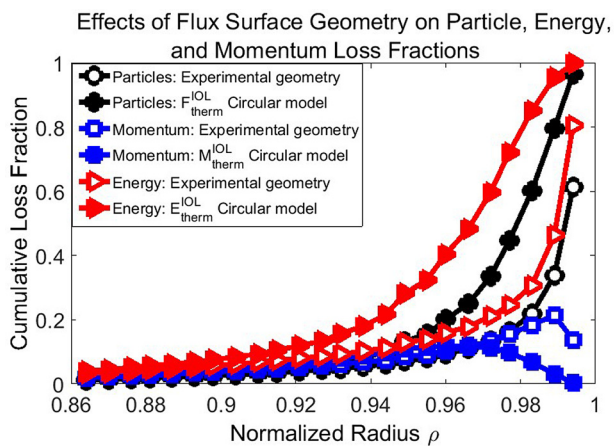


FIG. 6. Cumulative ion orbit loss particle, momentum, and energy loss fractions calculated with realistic geometry (empty symbols) and with an effective circular model (solid symbols).

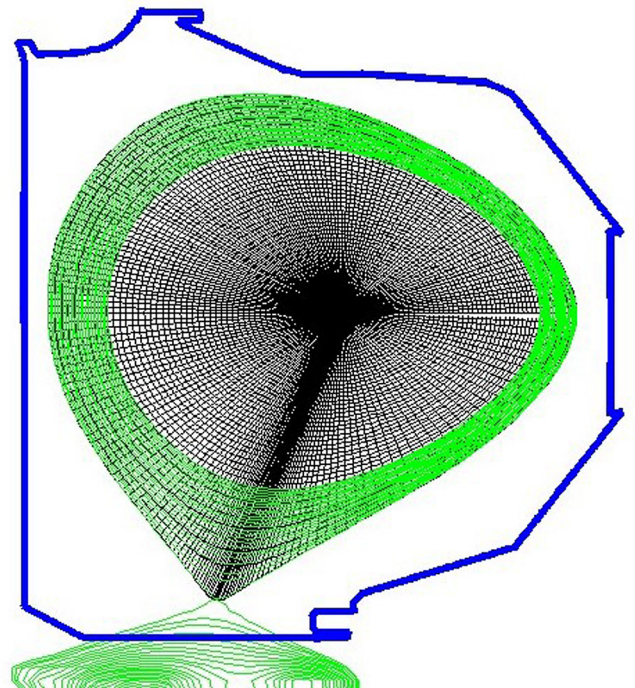


FIG. 7. Geometric mesh calculated using the analytical Miller model compared with experimental flux surface geometry.



the total number of particles that satisfy IOL requirements is unity, then no particles are ion orbit lost; if it is zero, then all IOL particles are removed from the plasma. In reality, the fraction lies somewhere in the middle. To investigate this further, the particle following code ORBIT<sup>41</sup> was used to perform a numerical study tracking particle trajectories outside of the separatrix in the DIII-D H-mode plasma shot #123302. It is assumed that if the particle orbit intersects with the vessel wall, then those trajectories are considered absolutely lost, whereas other orbits have the possibility of returning the ions to the plasma. Further analysis is required to extend this simulation to account also for processes that are occurring in the SOL such as charge exchange collisions with neutrals, which would remove particles from the plasma even if their trajectories do not intersect the wall.

For the present study, particle orbits were traced for 104 trial trajectories from 90 boundary points along the separatrix, at 5 different energies (100 eV, 500 eV, 1 keV, 3 keV, and 5 keV). The 104 different trajectories are shown for one boundary point in Fig. 8, where the (red) trajectories to the left represent particles launched away from the plasma core, and the (blue) trajectories to the right are towards the plasma core. The direction of each trajectory was chosen to sweep all angles with respect to the local toroidal magnetic field.

After calculating all the orbits, the fraction of ions that hit the wall was determined as a function of energy, shown in Fig. 9. It is interesting to note that very low energies have a large non-return fraction, then a threshold is reached where the non-return fraction drastically decreases before increasing at a slower monotonic rate through the keV energy range. The lower energy particles have a higher non-return fraction, which mostly occurs in the upper inboard quadrant. A potential cause for this is due to high energy particles drifting inwardly due to magnetic field curvature from neoclassical drifts, while the lower energy particles do not, and simply strike the wall (which is very close to the plasma in this region).

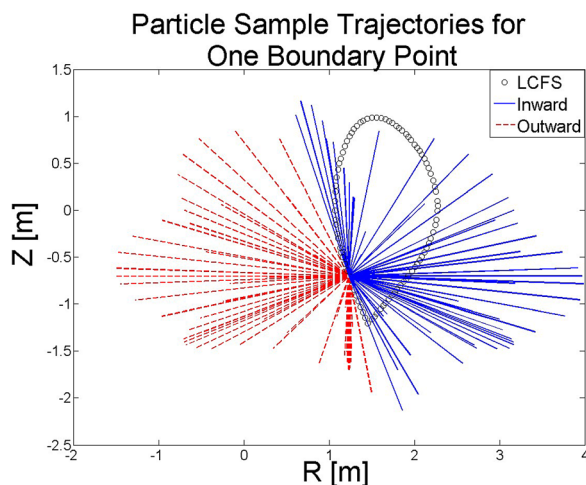


FIG. 8. Example of 104 initial velocity vector positions for a single boundary point on the separatrix. Particle trajectories based on these conditions were followed by a Lorentz solver to determine the fraction of particles that hit the wall using experimental DIII-D flux surface, magnetic fields, and wall geometry. (Blue) Launches to the right are towards the core and (red) launches to the left are towards the scrape off layer.

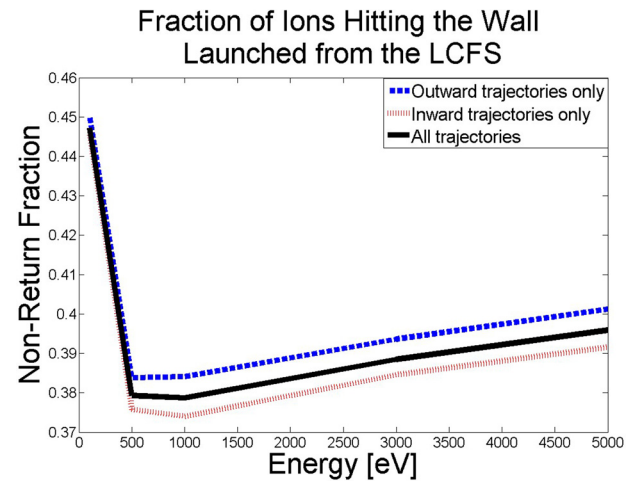


FIG. 9. Fraction of ions that hit the wall out of all trajectory trials as a function of energy.

This analysis shows that roughly 40% of ions that can energetically make it to the separatrix will strike the wall and be removed from the plasma. This fraction will be considered the “non-return” fraction,  $F_{NR} = 1 - R_{loss}^{IOL}$ . Of the other 60%, some may still be removed due to charge exchange or collisions with neutrals, but this must be explored further. The “outward trajectories only” curve represents the number of outward trajectories that intersected the wall divided by the total number of outward trajectories (dashed red lines in Fig. 8).

The non-return fractions can also be analyzed as a function of poloidal position, as shown in Fig. 10. There are spikes in fractions of particles striking the wall at the upper chamber wall located approximately at  $\theta = \pi/2$ , outboard midplane ( $\theta = 0$ ), and the divertor ( $\theta = 3\pi/2$ ). Losing particles at the top of the plasma is consistent with the close proximity of the plasma to the chamber wall at this location in DIII-D (see Fig. 7). Also consistent with losses at  $\theta = 0$  and  $\theta = 3\pi/2$ , previous IOL analysis<sup>34,42</sup> has predicted peaking in lost particles at the outboard midplane and an importance of x-loss<sup>43,44</sup> in the divertor region due to the null in poloidal magnetic field at the x-point.

When analyzing the poloidal dependence of losses at different energies, it is seen that the 100 eV energy ions exhibit larger variations in the non-return fraction than the 1 keV ions. The 1 keV ions have distinct loss peaks for the upper chamber wall and the divertor regions but appear to have consistent loss fractions for both the inboard and outboard sides of the plasma. The peak in the low energy non-return fraction in Fig. 9 is explained by the large increase in lost particles shown in Fig. 10(a) at the upper chamber wall of the vacuum vessel. These low energy ions do not have enough kinetic energy to neoclassically drift back into the plasma and strike the wall which is very close to the last closed flux surface at this poloidal location.

A similar analysis was performed for fast beam ions, but instead of launching particles from the separatrix, particle tracking was initiated along the outboard midplane, where the neutral beams are injected. Results showed that >90% of fast beam particles that are energetically allowed to execute



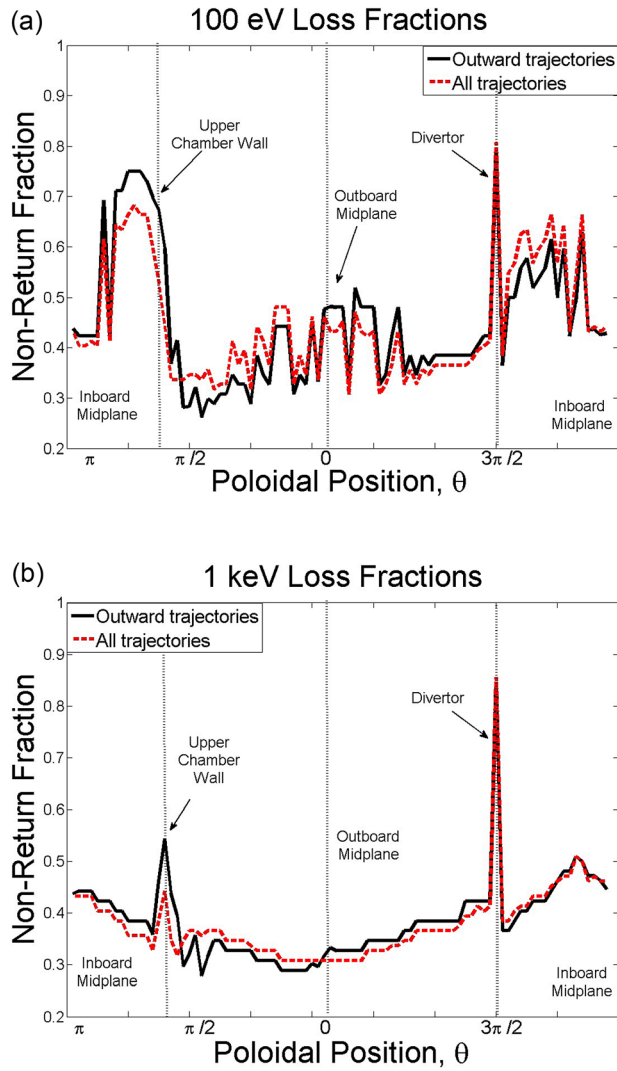


FIG. 10. Ion loss fractions as a function of poloidal position for (a) 100 eV ions and (b) 1 keV ions.

IOL orbits will hit the wall; therefore, the fast ion orbit loss fraction remains essentially unchanged.

An interesting outcome of this simulation was that fast ions began striking the wall (i.e., being ion orbit lost) in the ORBIT calculations at the same launch radius ( $\rho \approx 0.7$ ) for which the modified circular model first calculated NBI fast ion losses in Fig. 4 from conservation principles, validating this part of the fast beam IOL calculation.

### E. X-transport and x-loss

Another non-diffusive transport mechanism considered is called X-transport.<sup>43,44</sup> There is a region near the divertor x-point where the poloidal magnetic field becomes very small ( $B_\theta \ll \epsilon B_\phi$ ). In this region, the particle transport is different than in the rest of the plasma because the only magnetic field is in the toroidal direction, constraining particles to travel only in the toroidal direction with negligible poloidal displacement.

Because the ions are not spiraling poloidally, there are no neoclassical cancellations of velocity drifts, which allow ions to possibly drift out of the plasma through the x-point

before exiting this x-region. This was seen in the Lorentz force particle orbit simulation in Section II D by the spike in lost particles at  $\theta = 3\pi/2$  in Fig. 10.

The particle transport in this region is assumed to be collisionless and dominated by (a) poloidal  $\mathbf{E}_r \times \mathbf{B}_\phi$  drift and (b) vertically downwards curvature and grad-B drifts, which are described by Eqs. (13)–(15)

$$\bar{V}_{E \times B} = \frac{\bar{\mathbf{E}} \times \bar{\mathbf{B}}}{B^2} = \frac{E_r}{B_\phi} \hat{n}_\theta, \quad (13)$$

$$\bar{V}_{\nabla B} = \frac{W_{\text{perp}} \bar{\mathbf{B}} \times \nabla B}{eB^3} = \frac{W_{\text{perp}}}{eB_\phi^2} \frac{\partial B_\phi}{\partial R} \hat{n}_z, \quad (14)$$

$$\bar{V}_c = -\frac{W_{\text{par}} \bar{\mathbf{B}} \times \hat{n}_x}{eB^2 R} = \frac{2W_{\text{par}}}{eB_\phi R} \hat{n}_z. \quad (15)$$

$W$  is the ion energy in the parallel or perpendicular direction. During the time that the particle is inside the x-region, there is competition between these two drifts to transport the particle poloidally back into the plasma, x-transport to a different flux surface, or x-loss out of the plasma entirely, as depicted in Fig. 11.

If the poloidal drifts are sufficiently small, the ion will drift vertically downward across the separatrix through the x-point and be x-lost. In the far edge region where the radial electric field changes sign, the poloidal drift is reversed in the direction, allowing longer time periods for particles to be x-transported or x-lost due to the grad-B and curvature drifts. If the poloidal  $\mathbf{E} \times \mathbf{B}$  drift is dominant, then the ions will remain in the plasma but be x-transported to a flux surface closer to the separatrix. The plasma analyzed in this section has vertically downwards grad-B and curvature drifts; however, in a plasma with a grad-B drift in the radially inward

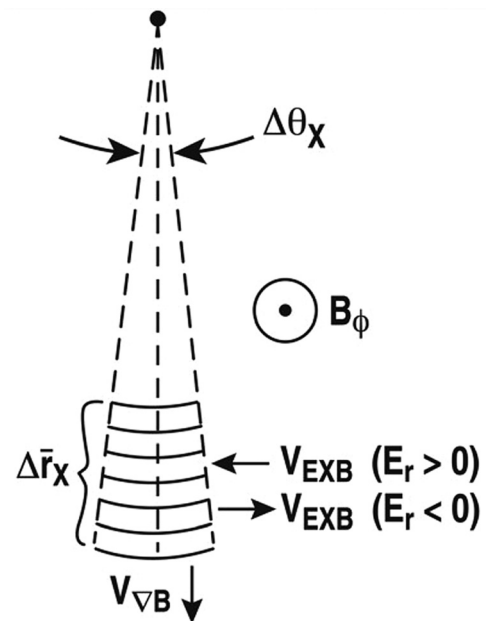


FIG. 11. Schematic of simplified circular model geometry for x-transport calculation. Reproduced with permission from W. M. Stacey, Phys. Plasmas **18**, 122504 (2011). Copyright 2011 American Institute of Physics.

direction, this model will not predict any x-loss and would describe x-transport in the radially inward direction.

Large scale Monte Carlo guiding center simulations have identified x-loss as a dominant source of non-ambipolar ion transport, and therefore an agent of a radial electric field generation in the edge region.<sup>43</sup> Previous models have developed x-transport theory with averaged time scales over the entire x-region using a modified circular model.<sup>44</sup> This research aims to extend the modified circular model theory by incorporating realistic geometry and particle tracking to determine realistic minimum energy values required for particles to be x-transported from an inner flux surface to each outer flux surface. Similar to ion orbit loss theory, minimum energy matrices for ions to be x-transported or x-lost can be used to develop a methodology for incorporating the non-diffusive transport mechanisms into edge fluid models.

The previous modified circular model<sup>44</sup> can be used to calculate the minimum energy required to x-transport ions from an inner flux surface to an outer flux surface using Eq. (16) as a constraint and assuming that ions with greater energy than the minimum energy,  $W_{min}^x(n \rightarrow m)$  can also be transported equally as far across flux surfaces

$$W_{min}^x(n \rightarrow m) = \frac{\Delta r_{n \rightarrow m} e R E_{rn}}{r_n \Delta \theta_x (1 + \xi_0^2)}. \quad (16)$$

The x-region has poloidal arc width,  $r \Delta \theta_x$ , and is divided into radial segments of width  $\Delta r_{n \rightarrow m}$  between flux surfaces  $n$  and  $m$ , traveling in direction  $\xi_0 = \cos\left(\frac{V}{V_{||}}\right)$  with respect to the magnetic field. This simplified circular model, whose geometry is illustrated in Fig. 11, will be used as a comparison to a more in depth particle tracking method developed for this research.

Extended x-transport methodology includes calculating the velocity field from the poloidal and vertically downward drifts and then tracking ion trajectories through the x-region due to the experimental magnetic field and radial electric field distributions. Particles that begin on flux surfaces on the left side of the x-region, as in Fig. 12, are moving in the co-current direction. Conversely ions are moving in the counter-current direction if they enter on the right side of the region. The poloidal ExB drift is dominant until the radial electric field approaches zero, and then the downward grad-B and curvature drifts have a greater effect. These downward drifts are the primary mechanism for x-transport to occur; however, the radial electric field becomes larger in magnitude at a rate rapid enough to keep some x-transported particles in the plasma instead of being lost through the x-point. This process can be assumed to be time dependent such that when no  $E_r$  shear is present, ions are easily x-lost, which acts to construct an  $E_r$  “well” whose shear constrains more x-transported ions to the plasma. In steady state, which is considered in this research, there will be a constant x-transport and x-loss associated with a particular  $E_r$  whose losses will be determined by the time scale of processes determining  $E_r$  and the compensating return currents. Figure 12 shows an example particle trajectory for a high energy ion. Lower energy ions will exhibit much smaller radial transport in the

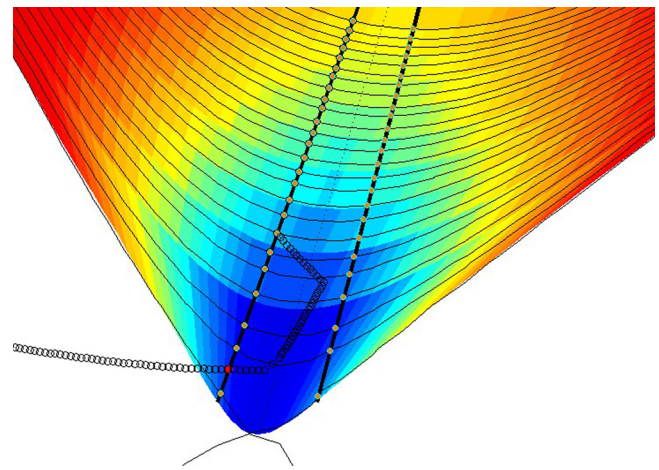


FIG. 12. The x-region of the tokamak showing a representative particle trajectory for  $\xi_0 = -0.5$  through the region. The dark blue region represents the nulled poloidal magnetic field.

x-region, especially in discharges with large radial electric fields driving the poloidal drift.

Using this model, a minimum energy matrix similar to the previous simplified circular geometry model in Table I of Reference 44 can be calculated describing how much energy is required for a particle on a given inner flux surface to be x-transported to a given outer flux surface or out of the plasma entirely. After analyzing x-transport for particles with pitch angle  $\xi_0 = \pm 0.5$ , results showed that even with extremely high energies up to 20 keV, particles were consistently x-transported, but not x-lost out of this particular H-mode DIII-D plasma, similar to the example trajectory in Fig. 12, which exemplifies an extreme case with very large radial displacement. Table I shows the corresponding minimum x-transport energy matrix for an ion to travel from one flux surface to another in the edge plasma for DIII-D H-mode shot #123302 and  $\xi_0 = \pm 0.5$  compared to the results obtained for the same pitch angles in Reference 44 using the simplified circular model. The format for data presentation in the table is: (modified circular model)/(particle tracking model). For example, according to Table I, the minimum energy required for an ion to be x-transported from  $\rho = 0.926$  to  $\rho = 0.932$  is 0.5 keV for the simplified circular model and 0.4 keV for the particle tracking model.

The minimum energy for the simplified geometry model is seen to monotonically increase for an ion to move farther out in the plasma, and minimum energy values can be calculated for all combinations of flux surfaces leading to an upper triangular matrix. This assumes a constant radial electric field within the mesh of the calculation. The particle tracking calculation accounts for a varying radial electric field across the ion trajectory. With the inclusion of this physics, the minimum energy matrix takes a diagonal form, suggesting that ions can primarily be x-transported to the  $n + 1$  flux surface and results in larger minimum energies to be x-transported in general. This suggests that x-loss, or the particle crossing the separatrix from this mechanism, occurs less frequently than a particle being x-transported to a flux surface closer to the separatrix.

TABLE I. Minimum energy matrix for an ion  $\xi_0 = \pm 0.5$  to be x-transported from one flux surface to another. Data format is: (Simplified Geometry Model)/(Particle Tracking Model). Energies are in keV.

$\rho$	0.932	0.938	0.943	0.949	0.955	0.960	0.966	0.972	0.977	0.983	0.989	0.944	1.00
0.926	0.5/0.4	4.6	2.5/X	4.0/X	5.8/X	8.0/X	10.4/X	13.2/X	16.2/X	19.4/X	>20/X	>20/X	>20/X
0.932		0.9/X	2.0/X	3.5/X	5.3/X	7.5/X	9.9/X	12.7/X	15.8/X	18.9/X	>20/X	>20/X	>20/X
0.938			1.1/4.1	2.7/8.0	4.5/>20	5.568.0	9.1/X	11.9/X	14.9/X	18.0/X	>20/X	>20/X	>20/X
<b>0.943</b>				<b>1.6/3.5</b>	<b>3.4/16</b>	<b>5.5/&gt;20</b>	<b>8.0/X</b>	<b>10.8/X</b>	<b>13.8/X</b>	<b>16.9/X</b>	<b>&gt;20/X</b>	<b>&gt;20/X</b>	<b>&gt;20/X</b>
0.949					1.9/12.2	4.0/>20	6.5/X	9.2/X	12.3/X	15.4/X	18.6/X	>20/X	>20/X
0.955						2.2/10.7	4.7/>20	7.4/X	10.5/X	13.6/X	16.8/X	19.7/X	>20/X
0.960							2.5/13.8	5.3/>20	8.3/X	11.5/X	14.6/X	17.5/X	20.0/X
0.966								2.8/16.7	5.9/>20	9.0/X	12.2/X	15.0/X	17.6/X
0.972									3.1/14.5	6.2/>20	9.4/X	12.2/X	14.8/X
0.977										3.2/15.6	6.3/>20	9.2/X	11.7/X
0.983											3.2/13.4	6.1/>20	8.6/X
0.989												2.9/10	5.4/>20
0.944													2.6/13

The third row in Table I ( $\rho = 0.932$ ) represents the flux surface where the radial electric field changes from positive to negative as illustrated in Fig. 1(b). When  $E_r = 0$ , there is no poloidal transport possible in the particle tracking model, so particles are not able to enter the x-region, which is why there are no minimum x-transport energies available on this flux surface for the particle tracking model (represented by an 'X'). However, in reality, ions with some poloidal inertia will transport into the x-region on this flux surface and experience an uncontested vertically downwards grad-B drift, which will produce a source of particles onto the flux surfaces outwardly adjacent to the flux surface where  $E_r = 0$ . The diagonal entries in Table I represent the most energetically favorable x-transport scenario for an ion to travel from flux surface  $n$  to  $n + 1$  and will subsequently be used in the fluid model.

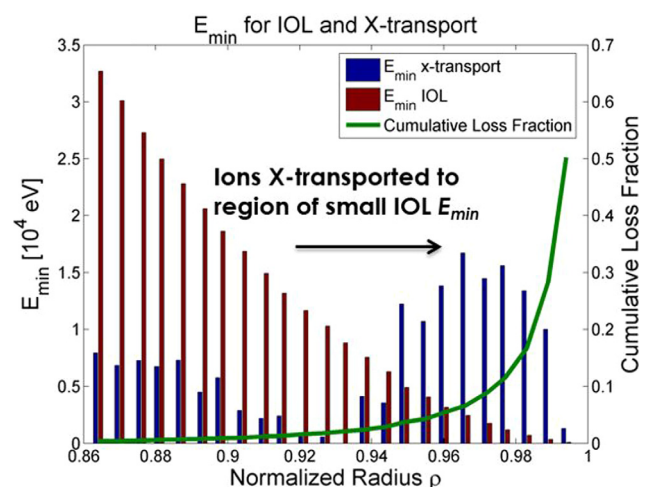
Assuming most particles are only energetically allowed to be x-transported one flux surface at a time towards the separatrix like a cascade, when an ion exits the x-region after being x-transported it re-enters the region of the tokamak with normal neoclassical transport occurring, it is swept around the flux surface and samples all possible locations and minimum energies for ion orbit loss before re-entering the x-region. This process puts conventional ion orbit loss in direct competition with x-transport for each flux surface, where IOL can happen at any poloidal location, but x-transport only occurs at roughly  $\theta = 3\pi/2$ .

The process that has the smallest minimum required energy allowing an ion to be transported either out of the plasma (IOL) or to the next flux surface (x-transport) will dictate the loss on that flux surface. To analyze which mechanism dominates, Fig. 13 shows a comparison of minimum energies for x-transport calculated from the particle tracking model and thermal ion orbit loss for edge plasma flux surfaces.

The minimum energy for thermal IOL is seen to monotonically decrease towards the separatrix. The minimum energy for IOL drops below that of x-transport at  $\rho = 0.943$ , making IOL more favorable in the outer edge region and x-transport more favorable in the inner edge region. This process of “x-transport pumping” causes lower energy particles

in the inner edge region (that were previously not energetically available to be IOL) to be pumped into a region where they are energetically allowed to be IOL. The bold row in Table I shows the flux surface where IOL becomes dominant. It can be seen that the minimum energies for x-transport become significantly larger for the particle tracking scheme at larger radii than this flux surface compared to the modified circular model due to the larger (but negative) radial electric field. This suggests that any model considering both IOL and x-transport processes must consider them as coupled. The cumulative ion orbit loss fraction profile is also shown in Fig. 13, illustrating that as the minimum energies required for ions to be lost is sufficiently decreased, the fraction of ions with a large enough energy to escape increases.

To be incorporated into the fluid equations, the mechanism for making up the lost charge from x-transport and its relationship with conventional IOL must be analyzed. Both IOL and x-transport act on the same ion velocity distribution on a given flux surface. However, there will be an extra source and sink due to x-transport for particles on each flux surface, as indicated in the continuity balance equation

FIG. 13. Comparison of minimum energy for co-current particles to be either x-transported or thermally ion orbit lost for a pitch angle of  $\xi_0 = \pm 0.5$ .



$$\nabla \cdot \Gamma_m = n_m \nu_{ion,m} + \hat{S}_{nbi,m} - 2\Gamma_{rj,m} \frac{\partial F_{therm,m}^{IOL}}{\partial r} + \sum_n F_x(n \rightarrow m) \Gamma_{rj,n} - \sum_{n'} F_x(m \rightarrow n') \Gamma_{rj,m}. \quad (17)$$

$F_x(n \rightarrow m)$ , which is applied to the radial particle flux on the initial flux surface  $n$ , is the loss fraction due to x-transport from flux surface  $n$  to flux surface  $m$  defined by taking the integral of velocity space similar to the IOL loss fraction from Eq. (5). When using the assumption that ions can only be x-transported across one surface, this sum will disappear and turn into a source from just the previous flux surface. The x-transport sink is similarly defined for the loss of particles on flux surface  $m$  due to x-transport to flux surface  $n'$  closer to the separatrix. In this continuity equation, either the thermal IOL sink or the x-transport sink apply depending on which process has the most favorable minimum energy.

To simplify this equation for realistic implementation in simplified fluid equations, the “x-transport pumping” process was utilized to model the x-transport directly into the thermal ion orbit loss fraction, allowing the continuity equation to remain unchanged (i.e., without the last two terms in Eq. (17)), but utilizing different  $F_{therm}^{IOL}$  curves. Assuming particles can only be transported to the next flux surface, the cumulative particle fraction shifts radially outwards by the integral over the different minimum loss energies between the two processes of IOL and x-transport

$$\Delta F_n^x = \frac{\int_{W_{min}^x}^{E_{min}^{IOL}} V_0^2 f(V_0) dV_0}{\int_0^\infty V_0^2 f(V_0) dV_0} = \frac{\left| \Gamma\left(\frac{3}{2}, W_{min}^x\right) - \Gamma\left(\frac{3}{2}, E_{min}^{IOL}\right) \right|}{\Gamma\left(\frac{3}{2}\right)}. \quad (18)$$

For both x-transport model analyses, average pitch angle directions of  $\xi_0 = \pm 0.5$  were taken into account in contrast to the cumulative thermal ion orbit loss calculation that accounts for all pitch angles. The primary goal of this calculation was to develop a more accurate x-transport calculation using the same theory as Reference 44 that can be incorporated into fluid balance equations. Full treatment of this mechanism would require a second integral over the directional cosine variable, which is an active area of future work.

Results from comparing the two models were used to develop assumptions for a simplified implementation into the fluid equations. It is assumed that all x-transported particles will cascade down to the flux surface where ion orbit loss becomes the dominant process, so there is a large source of relatively lower energy, counter-current particles that become newly available to be ion orbit lost. However, the majority of these ions will be immediately lost when this condition is met because low energy, counter-current particles are preferentially lost in the IOL process. Therefore, it is assumed that all of the “x-transport pumped” particles are lost to the plasma via the conventional ion orbit loss mechanism, but this happens on a flux surface closer to the separatrix ( $\rho = 0.943$  in this case) than where they were originally

displaced. Because these x-transported ions are actually lost via the IOL mechanism, they can be removed from the plasma by modifying the total loss fraction profile, instead of the particle source and sink terms in the continuity equation

$$F_{loss}^{tot} = \frac{F_{therm}^{IOL} + \sum_{n=1}^K \Delta F_n^x}{1 + N_{tot}^x / N_{tot}^{IOL}}. \quad (19)$$

$K$  is the flux surface where ion orbit loss becomes dominant, and the sum accounts for the total loss fraction,  $F_{loss}^{tot}$ , to be treated as a cumulative profile. The denominator accounts for the presence of more particles on each outer flux surface than originally due to x-transport, constraining the ratio of x-transported particles,  $N_{tot}^x$ , to total number of particles modifies this cumulative fraction to a maximum value of 1.

The x-transport modified cumulative loss profile compared to the conventional thermal ion orbit loss profile is shown in Fig. 14 for the DIII-D H-mode shot #123302 to be small relative to the thermal ion orbit loss, at least for this particular LSN discharge.

This restructuring of the cumulative loss fraction curves due to the competing processes of IOL and x-transport increases the particle loss fraction through the steep gradient region of the pedestal as expected. The effect would be amplified with the inclusion of all pitch angles (not just  $\xi_0 = \pm 0.5$ ), and this will be considered in future work.

### III. EFFECTS OF ION ORBIT LOSS MODEL IMPROVEMENTS ON CALCULATION OF RADIAL PARTICLE FLUX, INTRINSIC ROTATION, AND RADIAL ELECTRIC FIELD

Ion orbit loss model improvements can be included in fluid equations to calculate the (1) radial particle flux, (2) intrinsic rotation, and (3) radial electric field as described in Reference 20. The term “model improvements” refers to the four extensions to ion orbit loss theory previously discussed, which are the inclusion of fast beam ion orbit loss, the use of experimental flux surfaces and magnetic fields instead of a

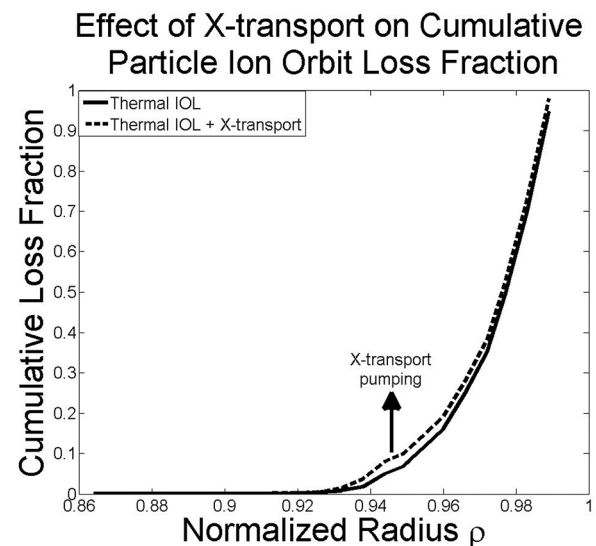


FIG. 14. X-transport corrected particle loss fractions for  $\xi_0 = \pm 0.5$  ions.

modified circular geometric model, the reduction of the amount of ion orbit loss calculated by 40% due to some ions returning to the plasma after executing orbits that cross the separatrix, and the inclusion of “x-transport pumping.”

The radial particle flux calculated from the first three terms on the right hand side of Eq. (17) is shown in Fig. 15, which compares the results with and without improvements to the IOL model as well as to the calculation with no ion orbit loss correction.

The (no IOL) radial particle flux without correction for ion orbit loss monotonically increases towards the separatrix because of the increasing ionization source due to recycling neutrals increasing towards the wall. However, when the radial ion particle flux is corrected for IOL, the flux decreases in the far edge region both because outflowing ions are lost by IOL and because of the negative sign of the inflowing ion current from the scrape off layer necessary to maintain charge neutrality. Inclusion of IOL model improvements further reduces the radial particle flux due to the effects of fast ion losses.

Model improvements to the IOL calculation affect the intrinsic rotation calculation from Eq. (7) as shown in Fig. 16. The use of experimental flux surfaces and magnetic fields appears to dominate the momentum calculation, causing the prediction of the intrinsic rotation peak to be larger and located closer to the separatrix relative to the peaking predicted by the circular model, which is consistent with experimental observation of peaking just inside the separatrix.<sup>29,45,46</sup>

The radial electric field is routinely calculated from experimentally measured carbon parameters by utilizing the carbon radial momentum balance equation

$$E_{rc}^{Exp} = \frac{1}{Z_c n_c} \frac{\partial p_c}{\partial r} - V_{\theta c} B_{\phi} + V_{\phi c} B_{\theta}. \quad (20)$$

Equation (20) evaluates the radial electric field profile in experiments; however, it does not identify the physical processes determining  $E_r$ . Previous research<sup>20</sup> has developed a modified Ohm’s Law which determines the radial electric

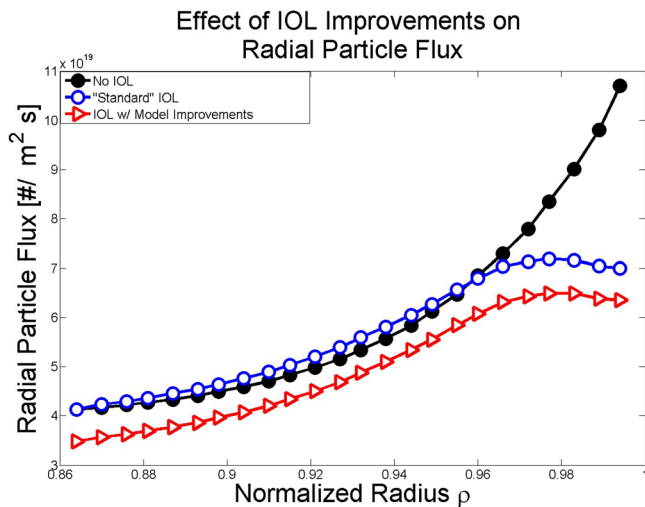


FIG. 15. Radial particle flux with and without ion orbit loss model improvements compared to the case without ion orbit loss.

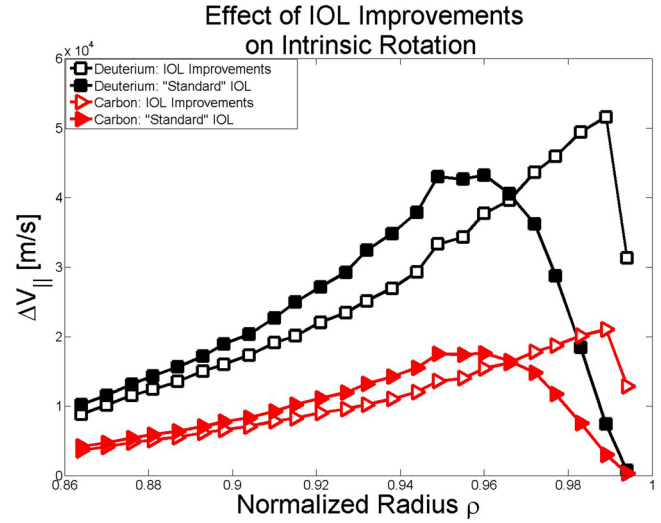


FIG. 16. Effect of flux surface representation in ion orbit loss calculations on intrinsic parallel rotation for both deuterium and carbon.

field from the combined effects of the deuterium, carbon, and electron species

$$E_r^{Ohm} = \eta_{\perp, Spitzer} j_r - (\mathbf{u} \times \mathbf{B})_r + \frac{1}{e_j(n_j + z_k n_k)} \nabla_r(p_j + p_k). \quad (21)$$

The first term is derived from the Lorentz collisional friction model, where the Spitzer perpendicular resistivity<sup>47</sup> is  $\eta_{\perp, Spitzer} = 1.03 \times 10^{-4} Z_{eff} \ln(\Lambda) / T_e^{3/2}$ , and the radial current  $j_r$  is required by charge neutrality to compensate for both fast and thermal ion orbit lost particles, as described in Section II.

In Fig. 17, the modified Ohm’s Law expression evaluated with experimental velocities (perturbation theory used for deuterium toroidal velocity<sup>48</sup>) is shown to adequately calculate the radial electric field for this H-mode discharge. With the IOL model improvements, the radial electric field “well” is shifted downwards and outwards. The “well” still

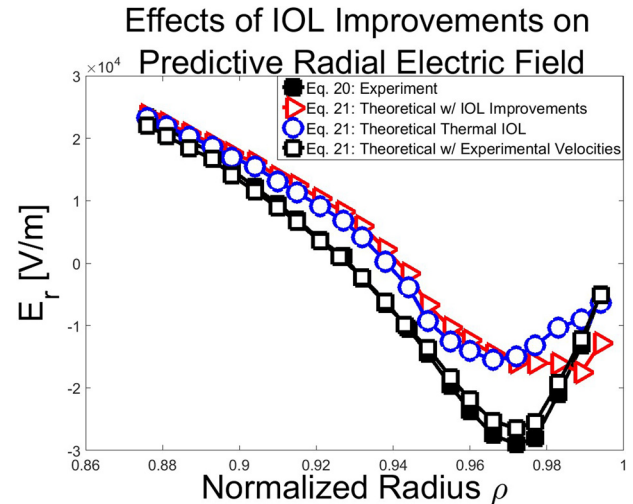


FIG. 17. Theoretical radial electric field with and without ion orbit loss model improvements compared to experiment. (DIII-D H-mode discharge #123302).

does not align directly with experiment, suggesting that the radial electric field model requires improvement in other areas outside of the ion orbit loss model such as extending the viscosity formalism to include effects of non-axisymmetry.<sup>49</sup>

## IV. CONCLUSIONS

An ion orbit loss model that can be included straightforwardly in fluid calculations has been significantly improved to account for fast neutral beam ion losses, as well as realistic flux surface and magnetic geometry and ions returning inward across the separatrix. The effects of ion x-loss and x-transport are also considered in this analysis through modification of the ion orbit loss fractions.

Prompt fast ion orbit lost particles act to reduce the radial particle flux profile directly due to a decreased source term in the thermalized ion continuity equation and indirectly due to an inward ion particle flux necessary to maintain charge neutrality. Using experimental magnetic fields and flux surface values in the ion orbit loss model decreases the predicted total amount of particle and energy losses relative to predictions using simpler magnetic field representations, while increasing the amount of momentum loss, as well as shifting the intrinsic rotation peak closer to the separatrix. This suggests that intrinsic rotation profiles could possibly be shaped through controlling the plasma elongation and triangularity.

A numerical study of orbit tracking predicts that roughly half of the particles that satisfy canonical angular momentum, magnetic moment, and energy balance requirements to be ion orbit lost will directly strike the wall. The other half have the opportunity to re-enter the plasma or may be removed from the plasma via a secondary mechanism such as charge exchange in the scrape off layer.

In-depth particle tracking in the x-region to analyze x-transport reveals a new mechanism, “x-transport pumping,” which transports (via grad-B and curvature drifts) lower energy ions on internal flux surfaces to outer flux surfaces where they are energetically able to be ion orbit lost. This effect can be included in the cumulative thermal ion orbit loss fraction for incorporation into the fluid equations but is expected to be small relative to conventional ion orbit loss. Applying the ion orbit loss model extensions to a theoretical fluid model for the radial electric field did not yield significant improvements, suggesting other areas of the model such as the viscosity formalism in the rotation models<sup>49</sup> need to be examined.

## ACKNOWLEDGMENTS

The authors are grateful to T. E. Evans of General Atomics for helpful discussions of this research. This work was supported in part by the U.S. Department of Energy under Grant No. FEFG01-ER54538 with the Georgia Tech Research Corporation.

<sup>1</sup>A. Hubbard, *Plasma Phys. Controlled Fusion* **42**, A15 (2000).

<sup>2</sup>J. E. Kinsey, G. Bateman, T. Onjun, A. H. Kritz, A. Pankin, G. M. Staebler, and R. E. Waltz, *Nucl. Fusion* **43**, 1845 (2003).

- <sup>3</sup>R. Aymar, V. A. Chuyanov, M. Huguet, Y. Shimomura, ITER Joint Central Team, and ITER Home Teams, *Nucl. Fusion* **41**, 1301 (2001).
- <sup>4</sup>M. Kotschenreuther, W. Dorland, Q. P. Liu, G. W. Hammett, M. A. Beer, S. A. Smith, and S. C. Cowley, in *Proceedings of the 16th Conference on Plasma Physics Controlled Fusion Research*, Montreal, 1996 (IAEA, Vienna, 1997), Vol. 2, p. 371.
- <sup>5</sup>J. E. Kinsey, R. E. Waltz, and D. P. Schissel, in *Proceedings of the 24th European Physical Society (Berchtesgarden, 1997)*, Vol. III, p. 1081.
- <sup>6</sup>T. H. Osborne, R. J. Groebner, L. L. Lao, A. W. Leonard, R. Maingi, R. L. Miller, G. D. Porter, D. M. Thomas, and R. E. Waltz, *Plasma Phys. Controlled Fusion* **40**, 845 (1998).
- <sup>7</sup>W. M. Stacey, R. J. Groebner, and T. E. Evans, *Nucl. Fusion* **52**, 114020 (2012).
- <sup>8</sup>W. M. Stacey, *Phys. Plasmas* **18**, 102504 (2011).
- <sup>9</sup>K. H. Burrell, *Phys. Plasmas* **4**, 1499 (1997).
- <sup>10</sup>P. W. Terry, *Rev. Mod. Phys.* **72**, 109 (2000).
- <sup>11</sup>K. H. Burrell, T. N. Carlstrom, E. J. Doyle, P. Gohil, R. J. Groebner, T. Lehecka, N. C. Luhmann, Jr., H. Matsumoto, T. H. Osborne, W. A. Peebles, and R. Philippon, *Phys. Fluids B* **2**, 1405 (1990).
- <sup>12</sup>K. H. Burrell, T. N. Carlstrom, E. J. Doyle, D. Finkenthal, P. Gohil, R. J. Groebner, D. L. Hillis, J. Kim, H. Matsumoto, R. A. Moyer, T. H. Osborne, C. L. Rettig, W. A. Peebles, T. L. Rhodes, H. StJohn, R. D. Stambaugh, M. R. Wade, and J. G. Watkins, *Plasma Phys. Controlled Fusion* **34**, 1859 (1992).
- <sup>13</sup>K. Ida, S. Hidekuma, Y. Miura, T. Fujita, M. Mori, K. Hoshino, N. Suzuki, and T. Yamauchi, *Phys. Rev. Lett.* **65**, 1364 (1990).
- <sup>14</sup>T. E. Evans, R. A. Moyer, P. R. Thomas, J. G. Watkins, T. H. Osborne, J. A. Boedo, E. J. Doyle, M. E. Fenstermacher, K. H. Finken, R. J. Groebner, M. Groth, J. H. Harris, R. J. La Haye, C. J. Lasnier, S. Masuzaki, N. Ohyabu, D. G. Pretty, T. L. Rhodes, H. Reimerdes, D. L. Rudakov, M. J. Schaffer, G. Wang, and L. Zeng, *Phys. Rev. Lett.* **92**, 235003 (2004).
- <sup>15</sup>T. E. Evans, R. A. Moyer, J. G. Watkins, T. H. Osborne, P. R. Thomas, M. Becoulet, J. A. Boedo, E. J. Doyle, M. E. Fenstermacher, K. H. Finken, R. J. Groebner, M. Groth, J. H. Harris, G. L. Jackson, R. J. La Haye, C. J. Lasnier, S. Masuzaki, N. Ohyabu, D. G. Pretty, H. Reimerdes, T. L. Rhodes, D. L. Rudakov, M. J. Schaffer, M. R. Wade, G. Wang, W. P. West, and L. Zeng, *Nucl. Fusion* **45**, 595 (2005).
- <sup>16</sup>J. S. deGrassie, R. J. Groebner, and K. H. Burrell, *Phys. Plasmas* **13**, 112507 (2006).
- <sup>17</sup>V. Rozhansky and M. Tendler, *Phys. Fluids B* **4**, 1877 (1992).
- <sup>18</sup>J.-P. Floyd, W. M. Stacey, R. J. Groebner, and S. C. Mellard, *Phys. Plasmas* **22**, 022508 (2015).
- <sup>19</sup>W. M. Stacey, *Phys. Plasmas* **20**, 092508 (2013).
- <sup>20</sup>T. M. Wilks and W. M. Stacey, “Calculation of the radial electric field from a modified Ohm’s law,” *Phys. Plasmas* (submitted).
- <sup>21</sup>F. L. Hinton and Y. B. Kim, *Nucl. Fusion* **34**, 899 (1994).
- <sup>22</sup>K. Miyamoto, *Nucl. Fusion* **36**, 927 (1996).
- <sup>23</sup>A. V. Chankin and G. M. McCracken, *Nucl. Fusion* **33**, 1459 (1993).
- <sup>24</sup>J. S. deGrassie, *Plasma Phys. Controlled Fusion* **51**, 124047 (2009).
- <sup>25</sup>P. Helander, R. J. Akers, and L.-G. Eriksson, *Phys. Plasmas* **12**, 112503 (2005).
- <sup>26</sup>W. M. Stacey, J. A. Boedo, T. E. Evans, B. A. Grierson, and R. J. Groebner, *Phys. Plasmas* **19**, 112503 (2012).
- <sup>27</sup>J. S. deGrassie, J. A. Boedo, and B. A. Grierson, *Phys. Plasmas* **22**, 080701 (2015).
- <sup>28</sup>T. Stoltzfus-Dueck, A. N. Karpushov, O. Sauter, B. P. Duval, B. Labit, H. Reimerdes, W. A. J. Vijvers, Y. Camenen, and the TCV Team, *Phys. Rev. Lett.* **114**, 245001 (2015).
- <sup>29</sup>W. M. Stacey and B. A. Grierson, *Nucl. Fusion* **54**, 073021 (2014).
- <sup>30</sup>D. J. Battaglia, K. H. Burrell, C. S. Chang, S. Ku, J. S. deGrassie, and B. A. Grierson, *Phys. Plasmas* **21**, 072508 (2014).
- <sup>31</sup>J. Seo, C. S. Chang, S. Ku, J. M. Kwon, W. Choe, and S. H. Müller, *Phys. Plasmas* **21**, 092501 (2014).
- <sup>32</sup>W. M. Stacey and T. M. Wilks, *Phys. Plasmas* **23**, 012508 (2016).
- <sup>33</sup>W. M. Stacey, *Phys. Plasmas* **23**, 062515 (2016).
- <sup>34</sup>W. M. Stacey and M. T. Schumann, *Phys. Plasmas* **22**, 042504 (2015).
- <sup>35</sup>A. Pankin, D. McCune, R. Andre, G. Bateman, and A. Kritz, *Comput. Phys. Commun.* **159**, 157–184 (2004).
- <sup>36</sup>J. Mandrekas, “Physics models and user’s guide for the neutral beam module of the supercode,” Report No. GTR-102 (1992).
- <sup>37</sup>L. L. Lao, H. S. John, R. D. Stambaugh, A. G. Kellman, and W. Pfeiffer, *Nucl. Fusion* **25**, 1611 (1985).
- <sup>38</sup>S. H. Müller, J. A. Boedo, K. H. Burrell, J. S. deGrassie, R. A. Moyer, D. L. Rudakov, and W. M. Solomon, *Phys. Rev. Lett.* **106**, 115001 (2011).
- <sup>39</sup>T. G. Collart and W. M. Stacey, *Phys. Plasmas* **23**, 052505 (2016).



- <sup>40</sup>R. L. Miller, M. S. Chu, J. M. Greene, Y. R. Lin-Lin, and R. E. Waltz, *Phys. Plasmas* **5**, 973 (1998).
- <sup>41</sup>R. B. White and M. S. Chance, *Phys. Fluids* **27**, 2455 (1984).
- <sup>42</sup>W. M. Stacey, *Nucl. Fusion* **53**, 063011 (2013).
- <sup>43</sup>C. S. Chang, S. Kue, and H. Weitzner, *Phys. Plasmas* **9**, 3884 (2002).
- <sup>44</sup>W. M. Stacey, *Phys. Plasmas* **18**, 122504 (2011).
- <sup>45</sup>J. A. Boedo, E. A. Belli, E. Hollmann, W. M. Solomon, D. L. Rudakov, J. G. Watkins, R. Prater, J. Candy, R. J. Groebner, K. H. Burrell, J. S. deGrassie, C. J. Lasnier, A. W. Leonard, R. A. Moyer, G. D. Porter, N. H. Brooks, S. Muller, G. Tynan, and E. A. Unterberg, *Phys. Plasmas* **18**, 032510 (2011).
- <sup>46</sup>C. Pan, S. Wang, and J. Ou, *Nucl. Fusion* **54**, 103003 (2014).
- <sup>47</sup>F. Trintchouk, M. Yamada, H. Ji, R. M. Kulsrud, and T. A. Carter, *Phys. Plasmas* **10**, 319 (2003).
- <sup>48</sup>W. M. Stacey and R. J. Groebner, *Phys. Plasmas* **15**, 012503 (2008).
- <sup>49</sup>K. C. Shaing, K. Ida, and S. A. Sabbagh, *Nucl. Fusion* **55**, 125001 (2015).